#### APPLIED SCIENCES AND ENGINEERING

# Electroluminescence of atoms in a graphene nanogap

Hyungsik Kim<sup>1</sup>, Young Duck Kim<sup>2,3</sup>, Tong Wu<sup>4</sup>, Qingrui Cao<sup>5,6</sup>, Irving P. Herman<sup>5</sup>, James Hone<sup>7</sup>, Jing Guo<sup>4</sup>, Kenneth L. Shepard<sup>1</sup>\*

Here, we report light emission from single atoms bridging a graphene nanogap that emit bright visible light based on fluorescence of ionized atoms. Oxygen atoms in the gap shows a peak emission wavelength of 569 nm with a full width at half maximum (FWHM) of 208 nm. The energy states produced by these ionized oxygen atoms bridging carbon atoms in the gap also produce a large negative differential resistance (NDR) in the transport across the gap with the highest peak-to-valley current ratio (PVR = 45) and highest peak current density (~90 kA/cm²) ever reported in a solid-state tunneling device. While tunneling transport has been previously observed in graphene nanogaps, the bridging of ionized oxygen observed here shows a low excess current, leading to the observed PVR. On the basis of the highly reproducible light emission and NDR from these structures, we demonstrate a 65,536-pixel light-emitting nanogap array.

Copyright © 2022
The Authors, some rights reserved; exclusive licensee
American Association for the Advancement of Science. No claim to original U.S. Government Works. Distributed under a Creative
Commons Attribution
NonCommercial
License 4.0 (CC BY-NC).

#### **INTRODUCTION**

Light emission from two-dimensional (2D) materials is of high current interest because of potential applications in optoelectronic devices. Much of this effort has focused on direct bandgap materials, such as WS<sub>2</sub> (1). Although bandgaps in these materials are generally more than 1 eV, producing light emission at wavelengths shorter than 600 nm has been difficult (2). 2D materials that have a bandgap (1, 2) have led to light-emitting diode structures in vertical heterostructures emitted primarily in the infrared (IR). Many of these efforts have focused on the search for direct wide-bandgap materials appropriate for efficient visible light emission, but finding direct bandgaps in excess of 1 eV has proven difficult. As an alternative, incandescent light emission (which is independent of bandgap) has been reported and studied in graphene. Incandescent light emission from graphene has a blackbody characteristic and can only be rendered visible in suspended structures that modulate IR emission from graphene (3); efficiencies are fundamentally poor—less than 10<sup>-5</sup>%. Chemically modified graphene, such as graphene oxides, has even been reported to emit visible light, although the EQE is very low (<0.1%) (3).

Graphene nanogaps, break junctions formed in patterned sheets of graphene, can be formed lithographically but have been shown to form when a graphene channel is damaged under high voltage bias to form the gap. In the latter case, the graphene sheets are generally fabricated in suspended structures (4). Transport in these cases has been argued to be by nanomechanical switching (5) effects or substrate interactions (6). Tunneling transport characteristics, including the presence of a negative differential resistance (NDR), have been observed in these devices, leading to investigations of the resulting hysteresis for switching applications (5, 7) as in the case for conventional tunnel diodes (8). Peak-to-valley ratios (PVRs) in these devices, a common figure of merit, have never exceeded 40 with peak current

density above 30 kA/cm<sup>2</sup> in these prior studies. This is less than what is achieved with resonant tunnel diodes fabricated in III-V heterostructures that have shown PVR values of up to 28 but with current densities of less than 1 kA/cm<sup>2</sup> (9).

Graphene nanogaps resemble metallic break junctions, which were initially introduced to contact single molecules to form single-molecule transistor (10). Metallic nanoparticles or roughened metal surfaces within these junctions have been shown to be electroluminescent (EL) (11, 12). Similar studies have been done using scanning tunneling microscopy (STM) tips, which are qualitatively similar in their spectral characteristics (13). A number of models have been put forward to describe the light emission in these systems, including inelastic tunneling excitation of optically coupled surface plasmon modes and nanoparticle quantum confinement.

Here, we report a graphene nanogap bridged by atoms of oxygen or nitrogen. Fabrication of these junctions is done in a unique manner, substrate-supported but with a graphene nanogap created by high-bias breakdown at vacuum levels on the order of  $\sim 10^{-4}$  torr. The electron transport in this case demonstrates NDR with a PVR in excess of 45 due to the notable lack of the excess current (due to direct thermionic emission) at high bias that characterizes most tunnel junctions, including other graphene nanogap studies. In addition, beyond the region of NDR, the junction atoms emit light, green light emission for oxygen and blue for nitrogen. Using this technology, we demonstrate an 8 mm-by-8 mm 65,536-pixel (256  $\times$  256) light-emitting array based on nonsuspended plasma-enhanced chemical vapor deposition (PECVD) graphene nanogaps, demonstrating the potential of this technology for EL displays. In these arrays, a single photoemission area is 1 µm<sup>2</sup>, and a unit pixel consists of 16 EL devices (arranged in a 4 × 4 array). Nonequilibrium Green's function (NEGF) modeling of these structures confirms the unique NDR characteristics associated with transport through ionized atoms.

#### **RESULTS**

#### **Device array fabrication**

We fabricated a  $256 \times 256$  array of 1- $\mu$ m-wide, 1- $\mu$ m-long exposed graphene two-terminal devices on the basis of PECVD graphene. PECVD allows for the wafer-scale deposition of uniform multilayered graphene without the need for catalysts, allowing the use of arbitrary growth substrates (14)—in our case, 4-inch Si/SiO<sub>2</sub> wafers as

<sup>&</sup>lt;sup>1</sup>Department of Electrical Engineering, Columbia University, New York, NY, USA. <sup>2</sup>Department of Physics, Kyung Hee University, Seoul, Republic of Korea. <sup>3</sup>Department of Information Display, Kyung Hee University, Seoul 02447, Republic of Korea. <sup>4</sup>Department of Electrical and Computer Engineering, University of Florida, Gainesville, FL, USA. <sup>5</sup>Department of Applied Physics and Applied Mathematics, Columbia University, New York, NY, USA. <sup>6</sup>Department of Physics, Carnegie Mellon University, Pittsburgh, PA, USA. <sup>7</sup>Department of Mechanical Engineering, Columbia University, New York, NY, USA.

<sup>\*</sup>Corresponding author. Email: shepard@ee.columbia.edu

shown in fig. S1A, PECVD graphene on 285-nm  $SiO_2$  has a bluish hue as opposed to the purple color of 285-nm  $SiO_2$ . Back-gating is possible through the highly p-doped Si substrate. These as-grown multilayer PECVD graphene layers had a thickness of 5 nm with sub–1-nm surface roughness (see text S1 and figs. S2 and S3). After growth, we diced the wafer into 20 mm–by–20 mm chips and used the chips for our fabrication. Figure S1B shows the Raman spectrum of the PECVD graphene, displaying higher defect levels than conventional CVD graphene at 2D (2690 cm $^{-1}$ ) and D + D' (2950 cm $^{-1}$ ) as well as a D (1350 cm $^{-1}$ ) peak higher than that generally observed with CVD graphene (15). These defects produce p-type doping as evidenced by a strong positive shift of the Dirac point under backgate bias (16).

Figure 1A shows the nonsuspended two-terminal devices shown in fig. S4, before nanogap formation, fabricated on the as-grown PECVD graphene films. To minimize contamination during fabrication, we used 20 mm-by-20 mm substrates, while the active device area is only the center 8 mm by 8 mm, accommodating the entire array as shown in Fig. 1 (C and D). The limited number of pins on the chip carrier restricted operation of our device to a small subset of pixels. Figure 1 (A to D) shows the device from the single element to the level of the fully packaged array. Figure 1A shows a single pixel of the nonsuspended graphene light emitter with a 1  $\mu$ m-by-1  $\mu$ m active graphene area. The bright point in the red dashed box of Fig. 1D is light emission from  $16 \times 4$  pixel array as shown in Fig. 1F. These particular devices were hermetically sealed with a cover glass under vacuum before nanogap formation.

## Nanogap formation and green color emission

The characteristics of light emission from a representative device having a configuration in Fig. 1E with width of 5 µm and length of 5 μm are shown in Fig. 1G (I and II) (see also movie S1) as it is biased between source and drain  $(V_{SD})$  in vacuum to pressures of approximately  $10^{-4}$  torr. In this initial biasing,  $V_{SD}$  is increased from 0 to 12 V at a rate of approximately 0.2 V/s (Fig. 2A). The device first shows incandescent illumination in the red distributed over the entire device area with the thermal distribution of the carriers (in this case, holes) in the graphene reaching temperatures up 2000 K, as determined by Planck's law (see text S2 and fig. S5) with a peak wavelength of 655.2 nm (Fig. 2B), although it is expected that the carriers are not in equilibrium with the temperature of the lattice (17). Thermal energy is transferred from the carriers to the lattice through both electron-phonon interactions and defect scattering. These nonsuspended structures conduct heat faster than suspended structures as direct thermal conduction to the substrate (such as SiO<sub>2</sub>) is far more efficient than radiative heat transfer through vacuum, probably further enhancing the disparity between carrier and lattice temperatures. For a representative device, at  $V_{\rm SD}$  of approximately 11.9 V (as shown in Fig. 2A), which we refer to as the "transition voltage," the current through the device abruptly drops and the red blackbody light emission stops. This happens as the lattice temperature at the center of the device leads to the formation of a nanogap. We believe that this happens away from the source and drain electrodes because of the additional heat sinking provided by the contacts. As shown in Fig. 1G, the red-light emission over the entire graphene channel is replaced by green light emission that now occurs at discrete points along the nanogap.

The green light emission spectrum (Fig. 2B) exhibits a peak at 569 nm with a 208-nm full width at half maximum (FWHM).

Blackbody emission at this wavelength would require temperatures in excess of 8000 K (see text S2 and fig. S5), while the devices shown here the carriers reach temperatures of only 2000 K (17) before nanogap formation, supporting the conclusion that this light emission is not incandescent in nature. In addition, while it was previously observed that optical interference effects can transform blackbody radiation in the near IR (NIR) into tunable peaks in the visible range (1) in suspended monolayer graphene samples, the emission spectra in this case still preserve the characteristics of blackbody radiation, including a prominent NIR (>700 nm) component (1), which is not observed in the spectrum of Fig. 2B for our nonsuspended samples.

In the current-voltage (I-V) characteristics of Fig. 2A, when ramping in the forward direction, red blackbody radiation starts at ~9 V and reaches peak intensity at ~11 V. At the transition voltage of 11.9 V, the green light emission begins as the current decreases sharply from 4.39 mA to 180 µA and the resistance of the device increases markedly from ~2.7 kilohms to a few gigaohms. The *I-V* characteristics are symmetric with respect to both negative and positive  $V_{SD}$ , before and after the nanogap formation, as shown in Fig. 2 (C and D). After initial nanogap formation in Fig. 2A at a transition voltage of 12 V, the voltage biases at which the I-V characteristic show that NDR reduces to between approximately 7.0 and 8.2 V. In Fig. 2 (C and D), which show I-V characteristics before and after nanogap formation, voltages are swept from 0 to 10 to -10 V and then back to 0 V. More details of the *I-V* characteristic changes are shown in figs. S6 and S7 (see text S3). Beyond the transition voltage, the emitted light occurring at discrete points in the nanogap changes nonmonotonically by up to 150% as the bias is increased to 20 V (see fig. S8). The current through the device does not significantly change. When the voltage bias is subsequently reduced, light emission ceases at 8.7 V, 3.2 V below the turn-on voltage. Below 7.0 V (Fig. 2D), the current in the device recovers to the values observed in the forward sweep with no incandescent or green light emission. In all subsequent sweeps (Fig. 2D), as the voltage magnitude increases beyond the NDR bias region (8.2 V), green light emission is produced; this persists until the voltage is reduced below the NDR bias region (7.0 V). Similar I-V characteristics and light emission properties were observed over more than 100 devices measured with varying widths and lengths. These I-V characteristics all show NDR characteristics. We find that the transition voltage varies linearly with channel length as shown in fig. S9A but is relatively independent of channel width (fig. S9B) and is relatively insensitive to back-gate bias (fig. S10).

I-V characteristics and green light emission after nanogap formation show remarkable endurance. Figure S11 shows variation in the I-V characteristic with multiple sweep cycles, showing small variations in the current values as a given value of  $V_{\text{SD}}$  from sweep to sweep. These are accompanied by similar fluctuations in the intensity of the green light emission. We attribute these variations to electromigration of the oxygen atoms in the gap. Figure S12 shows the drain current as a function of time in the "forward" and "reverse" states for the same device as fig. S8. Small fluctuations in the current are observed, but the device is robust for over 24 hours, showing continuous green light emission.

We note that the green light emission observed in the nanogap (Fig. 1G) is not dependent on substrate or on the polycrystalline nature of the PECVD graphene channel or its multilayer structures. In fig. S13, we cover the  $SiO_2$  substrate with hexagonal boron nitride (h-BN) and see no effect on the green light emission from PECVD

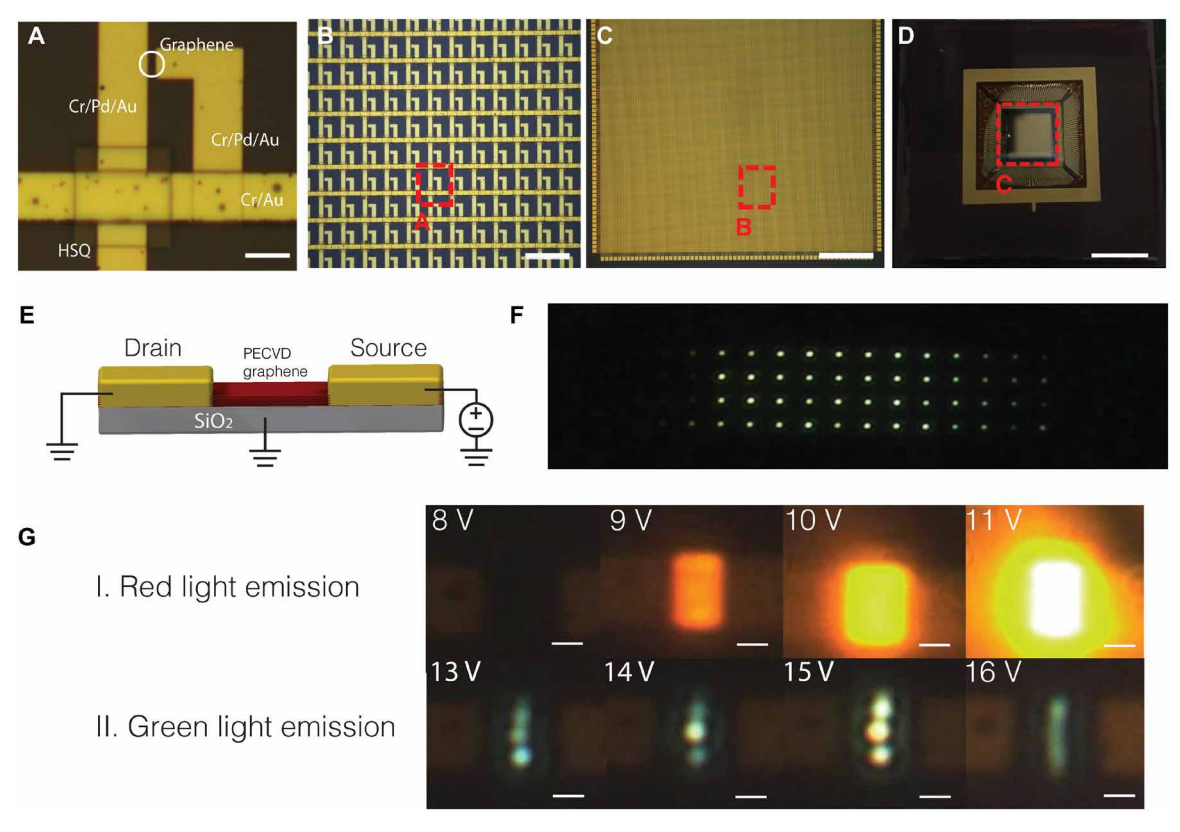


Fig. 1. Large-scale light emission array and light emission. (A) Image of a single pixel with  $1 \mu m^2$  of graphene (circled in white). Cr/Pd/Au and Cr/Au were used for contact and cross electrodes, respectively. Hydrogen silsesquioxane (HSQ) is used as an insulator to separate cross electrodes from contact electrodes. Scale bar, 5  $\mu$ m. (B) An array image including (A) in red dashed box. Scale bar, 50  $\mu$ m. (C) An array image including (B) in red dashed box. Scale bar, 1 mm. (D) A fully packaged chip on a 128-pin ball grid array. Scale bar, 10 mm. (E) A device configuration to analyze light emission. (F) Light emission from  $16 \times 4$  pixel array. (G) Light emission from array, thermal radiation, and green light emission. Light emission before (right top row) and after (right bottom row) nanogap device formation in  $W = 5 \mu$ m and  $L = 5 \mu$ m. Scale bars, 2  $\mu$ m.

graphene in either spectrum or intensity (see text S4). It is well known that the substrates underneath the graphene influence the transport characteristics (18, 19). The differences observed here between h-BN and SiO<sub>2</sub>/Si substrates have to do primarily with substrate thermal conductivity. hBN is much more thermally insulating, allowing the lattice temperature to equilibrate more easily with the carrier temperature, leading to lower transition voltages. In fig. S14, we show that the same NDR characteristics and green light emission are observed on monolayer graphene sample on Si/SiO<sub>2</sub> substrates (see text S5). Figure 1 GII shows the resultant green light emission over the entire array of these devices (see also movies S2 to S4) in the fully packaged chip.

# Graphene characteristics after nanogap formation

Microscope images after nanogap formation shown distinct changes in the surface morphology on either side of the nanogap (fig. S15), which is also reflected in the diagram of Fig. 3A. As shown in Fig. 3B, atomic force microscopy (AFM) and Raman mapping data confirm the different morphology and chemical composition on the two sides of the gap. Figure S16 shows that Raman data as the nanogap is forming. The D and G peaks in the drain side of the nanogap merge together compared with the distinct peaks on the right side, reflecting the higher lattice temperature reached on the drain side during nanogap formation, resulting in the formation of reduced graphene oxide (RGO) there. It is natural for the drain side to reach

higher temperature because the carriers are also hottest on the drain side of the channel. As a result, we believe that nanogap formation occurs with a lattice temperature around that required to oxidize graphene or approximately 700 K (20). From AFM data, pristine PECVD graphene has an initial roughness of 551 picometer (pm) root mean square (rms). After nanogap, formation, the RGO roughens to 1590 pm rms while the graphene on the source side smooths to 188 pm rms, as shown in Fig. 3 (C to E). Transmission electron microscopy images (fig. S17) confirm that the drain side of the nanogap has a thick oxide layer, three times thicker than the graphene layer (15 layers or ~5 nm thick) on the source side (see text S6). We attribute the smoothing on the source side to electromigration of grain boundaries from the source to the drain side as observed in plasma-treated graphene and adsorbate migration in graphene (21–23). AFM images of the nanogap (fig. S25) suggest gap sizes between 1 and 20 nm.

X-ray photoelectron spectroscopy (XPS) data (see text S7) allow us to discern a notable increase of C—O—C bonding in the graphene nanogap array (see table S1), similar to what is observed with oxygen annealing in a furnace as shown in fig. S18. The XPS data cannot distinguish the exact composition of each channel layer due to the large beam size (diameter of >100  $\mu$ m). The RGO forms despite the fact that the experiments are conducted in vacuum at  $10^{-4}$  to  $10^{-7}$  torr. While the SiO<sub>2</sub> substrate could be considered as the source of the oxygen (18, 19, 24), we rule this out because the

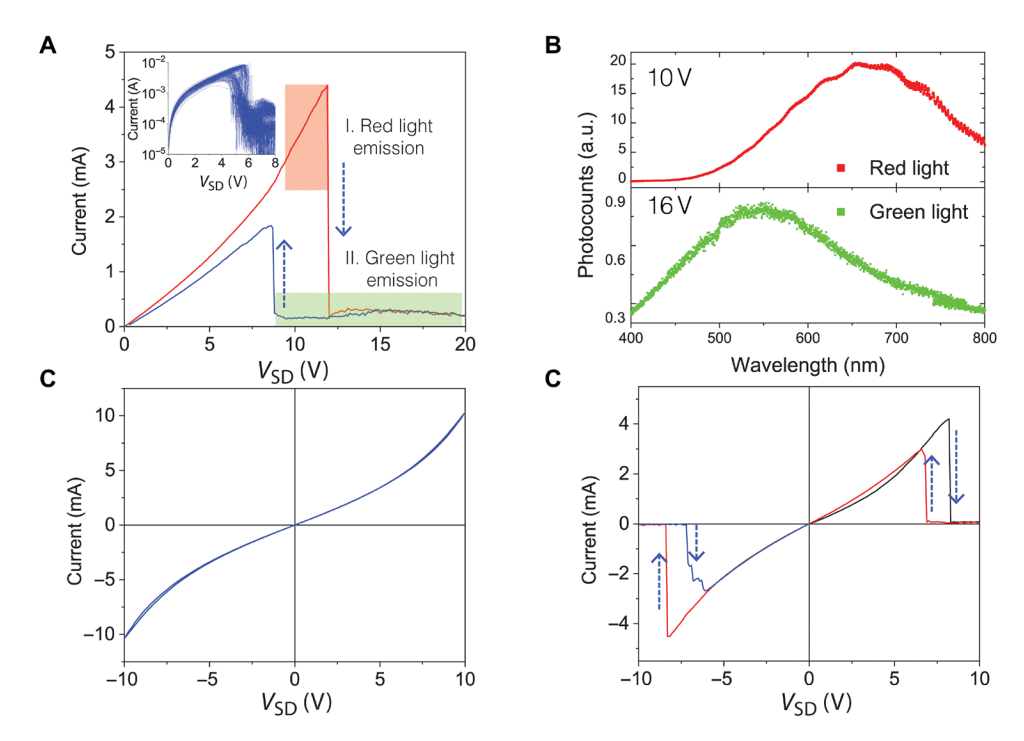


Fig. 2. Current-voltage (*I-V*) characterization and EL of the thermal radiation and green light emission. (A) *I-V* characterization in  $W = 5 \, \mu m$  and  $L = 5 \, \mu m$  when nanogap is formed. In the forward direction of bias voltage (red line), nanogap is formed in the current drop. Light emission is shown as shaded color boxes in the graph. Before the current drop, red light emission is observed in the low current level. Backward sweep of bias voltage still shows green light emission until the current increases up to the original current level (blue line). Inset: A hundred times sweep in  $W = 7 \, \mu m$  and  $L = 3 \, \mu m$ , which shows stable performance. (B) EL of the thermal radiation and green light emission. Light spectrum of the nanogap device showing a peak at 569.4- and 208.4-nm FWHM in green color emission at 16 V in the bottom and showing a peak at 655.2- and ~174.2-nm FWHM in thermal radiation at 10 V in the top. a.u., arbitrary units. (C and D) Symmetric *I-V* characteristic before (C) and after (D) the nanogap formation. After nanogap formation in (A) having a transition voltage of 11.9 V, the voltage range over which the *I-V* characteristic shown NDR characteristics is reduced up to 7.0 to 8.2 V. Green light emission occurs when the voltage magnitude is increased beyond 8.2 V and stops when the voltage magnitude drops below 7.0 V.

same effects are observed when h-BN substrates are used. We instead attribute this oxidation to residual oxygen in the chamber. This becomes more evident when we observe in fig. S19 that GRO formation, NDR in the I-V characteristics, and green light emission from the gap are not observed at vacuum levels of  $10^{-9}$  torr. For vacuum levels worse than  $10^{-3}$  torr, no current is observed across the gap.

The addition of electrodes E1 and E2, in addition to the source (S) and drain (D) electrodes in Fig. 3F, allows one to individually characterize the resistance of the bulk drain side, bulk source side, and nanogap as shown in in Fig. 3G. As expected, the nanogap I-V characteristics measured from E1 and E2 electrodes (Fig. 3G, inset) show the same NDR characteristics observed from the S and D contacts. Back-gate sweeps from the highly p-doped Si substrate (Fig. 3H) confirm hole conduction across the nanogap and in the bulk regions. We estimate the hole concentration to be  $1.47 \times 10^{12}$  cm<sup>-2</sup> and  $4.79 \times 10^{12}$  cm<sup>-2</sup> in the graphene and RGO, respectively, in the representative devices of Fig. 2 (25).

## **DISCUSSION**

Light emission and NDR observed in metallic break junctions have generally been attributed to quantum dot materials with tunneling transport characterized by models, which include the presence of an excess current determined by direct thermionic transport over the tunneling barrier (see text S8). Tunneling transport theoretically or

experimentally observed in other nanogap structures has shown this excess current (6, 26, 27). In our case, this excess current is noticeably suppressed or absent even at biases in excess of 10 V beyond the NDR peak. We comment also that this nanogap represents a previously unidentified type of NDR device that is neither of the N- nor S-type. NDR characteristics here show large peak-to-valley current ratios ( $I_p/I_v \sim 45$ ), vastly exceeding values observed in devices made in in GaAs (~28), Ge (~8), or Si (~4) (9, 28), and the highest peak current density (~90kA/cm²) reported from any device showing NDR as shown in fig. S20.

We hypothesize that the observed I-V characteristics, particularly the lack of an excess current beyond the NDR peak, are the result of tunneling through discrete states in a quantum well defined by weak coupling to atoms of oxygen. The quantized energy states ( $E_n$ , denoted with index n) inside a quantum well are given by

$$\Delta E = E_n - E_{cw} = \frac{h^2 n^2}{8 m^* W^2}$$

where h is Planck's constant,  $m^*$  is the effective mass of the electron,  $E_{\rm cw}$  is energy of the conduction-band-edge well, and W is the width of the potential well. For W defined by atomic dimensions,  $\Delta E$  is on the order of 2 eV, allowing only two or three states in the well before the vacuum level is reached as shown in fig. S21. Optical emission can come from transitions between these quantum-defined states, as populated by tunneling from the graphene.

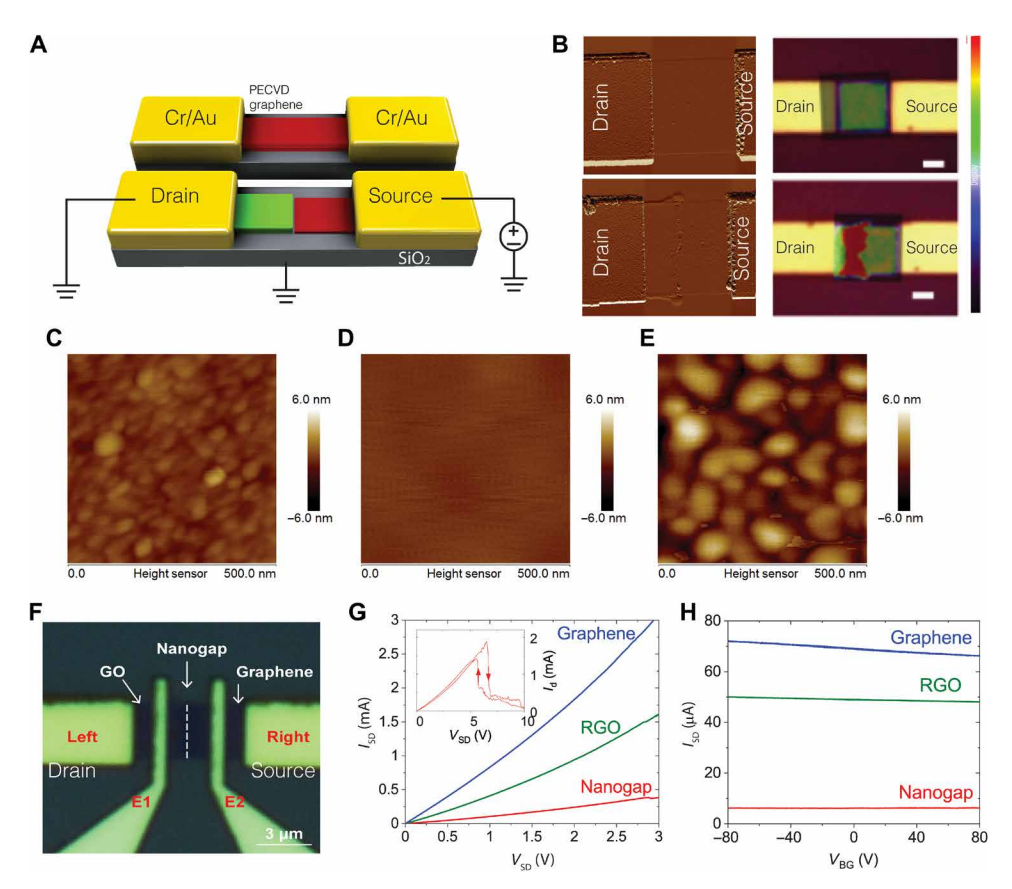


Fig. 3. Left and right side in the nanogap. (A) Device configuration before (top) and after (down) nanogap formation. (B) Atomic force microscopy (AFM) images and Raman mapping images in the graphene channel before and after the nanogap formation. Scale bars, 2.5  $\mu$ m. The color scale bar indicates that G peak (1583 cm<sup>-1</sup>) Raman intensity variation. (C to E) AFM images of pristine PECVD graphene (C), left side of nanogap (D), and right side of nanogap (E) in the area of 500 nm by 500 nm. (F to H) Graphene oxide transport. Microscope image (F) of a nanogap device having  $W/L = 3/5 \mu$ m. I-V characterization (G) and back gate dependence at  $V_{SD} = 100 \text{ mV}$  (H) in the area of graphene (E2 right electrode), nanogap (E1 and E2 electrode), and graphene oxide (GO, E1 left electrode), respectively.

To confirm our hypothesis, we conduct density functional theory (DFT) simulations (see text S9). Following theoretical work on how impurities in carbon chains change electron transport (29), we model the nanogap as weakly bonded oxygen atoms between two carbon chains, where the gap size between the carbon and oxygen is varied. Metal contacts assumed on a few carbon atoms at the far ends of each chain and two oxygen atoms are weakly bonded with two carbon chains to form the gap. This model is fundamentally based on a multiquantum well (MQW) structure but differs from other MQW transport formulations in that the width of the well is defined by the atomic dimensions of oxygen.

The MQW model shown in fig. S21 (A and B) can be used to both quantitatively and qualitatively explain the experimentally observed *I-V* characteristics (fig. S21C). At zero bias, the Fermi level is above the neutrality point of the highly p-doped graphene of the contacts and under the first energy state (E1) in the multiquantum well. With increasing bias voltage, the reflected electron ratio is at first high due to the low transmission ratio. When the quasi-Fermi level at the source reaches the first energy state (E1), current increases with low resistance because of the high transmission ratio through the quantum well at this bias. Until the Fermi level reaches the second energy state (E2), the current increases with increasing bias as shown in fig. S21 (C and D3). As shown in fig. S21 (C and D4), after the quasi-Fermi level at the source passes the second energy

state (E2), electrons injected from the source are able to recombine with hole injection from the drain, leading to green light emission ( $\sim$ 2.3 eV). At this bias point, the current abruptly drops because the second energy state (E2) is very close to the vacuum level. While this model assumes two coupled quantum wells due to the presence of two oxygen atoms in the gap, there are more oxygen atoms likely present, which is consistent with the measured EL spectrum that shows a very broad FWHM, as shown in Fig. 2B, consistent with a statistical distribution of quantum well structures of varying parameters. Measured I-V characteristics as shown in Fig. 2B and fig. S11 represent the sum of the current flowing through many quantum well structures in the gap.

Figure 4A shows a quantitative DFT calculation of the same nanogap structure with two oxygen atoms between carbon atoms (with additional details in fig. S22). As shown in fig. S23A, a simple circuit scheme can be idealized for calculation of I-V characteristics. Nanogap resistance  $R_{\rm n}$  was extracted from DFT calculation (fig. S23B), and, using this value of Rn, total resistance in the circuit can be calculated. Despite the limitations of this simple model, the simulated I-V characteristics, shown in Fig. 4A, match experiment reasonably well. To explain the light emission, we first note that the measured EL spectrum can be reconstituted with three broadened symmetric emission profiles at 483, 557, and 727 nm (Fig. 4B).

As is known generally in atomic spectroscopy, oxygen atom emits green light [and nitrogen emits blue light (30)] when excited. These

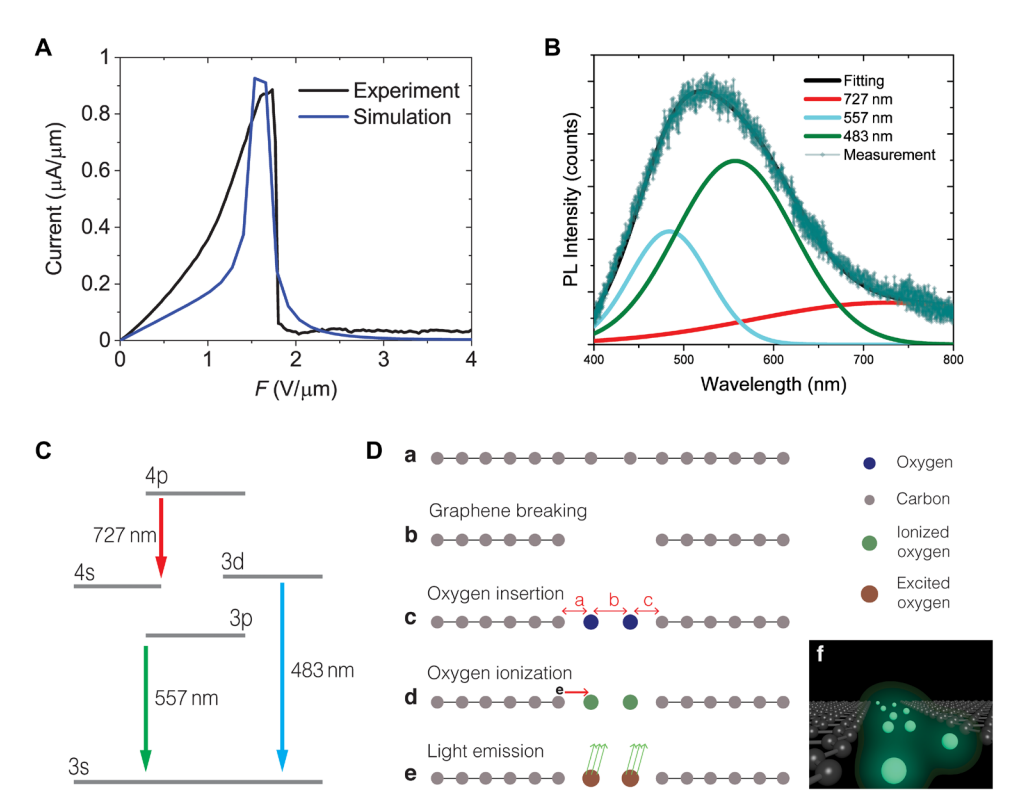


Fig. 4. Electrical and optical properties, and mechanism. (A) Electrical characterization. Simulated and experimental *I-V* characteristics. (B) Emission spectra. Light spectrum of the nanogap device showing a peak at 569.4- and 208.4-nm FWHM in green color emission is deconvoluted into 727, 557, and 483 nm. PL, photoluminescence. (C) Energy level and electron transition; 727, 557, and 483 nm come from the transition of 4p to 4s, 3p to 3s, and 3d to 3s, respectively. (D). Mechanism of green light emission. (a) A graphene state before breaking. (b) Graphene breaking by high temperature. (c) Oxygen atoms are located between two split graphene. (d) Hot electrons ionize oxygen atoms. (d and e) Doubly ionized oxygen atoms emit green light. (f) 3D rendering of a single pixel nanogap device.

particular spectral lines are associated with emission from doubly ionized oxygen [O++(O III)] and singly ionized oxygen O2++ (O II) (31). In particular, these transitions are  $2s^22p3p \rightarrow 2s^22p3s$  (557 nm),  $2s^22p4p \rightarrow 2s^22p4s$  (727 nm), and  $2s^22p3s \rightarrow 2s^22p3d$  (483 nm), as shown in Fig. 4C. Much of the spectral broadening of the light emission observed in Fig. 1G, we attribute to the presence of multiple light emission points within the gap with variability in the formations of oxygen atoms in the gap and with the carbon atoms contacting them (32), as shown in figs. S24 and S25. Light emission similar to that reported here has been observed for atoms caught between an STM tip and a substrate (33). Frequency shifts in the emission wavelength result from variations in the bonding to the contact.

Figure 4D shows the mechanisms of nanogap formation and light emission. After nanogap formation, oxygen atoms within the nanogap are ionized, resulting in the significant drop in current in Fig. 4A at a voltage of ~1.8 V/ $\mu$ m. The current peak in Fig. 4A corresponds to a power density of ~1.15 × 10<sup>9</sup> W/cm², which matches well the photoionization power density required to ionize molecular oxygen (~1 × 10<sup>9</sup> W/cm²) (34). In high vacuum pressures of more than 10<sup>-9</sup> torr, we observe excess tunneling current (fig. S19) and no light emission, indicating the importance of oxygen to the effects observed here. Figure 4D (a to f) shows a representation of a single nanogap device with multiple oxygen atoms within the gap.

This same mechanism also explains the blue light emission observed in nitrogen-doped graphene nanogaps, as shown in fig. S26 (see text S10). N-doped graphene displays a slightly higher transition

voltage than PECVD graphene but results in nitrogen, rather than oxygen, in the nanogap because of the relative abundance of nitrogen in the nitrogen-doped graphene.

To extract external quantum efficiency (EQE) of our devices, we need to estimate the emission area. For N atoms in the gap, we can estimate an emission area of  $N\pi r^2$ , where r is oxygen atom's radius. In this way, and the EQE is estimated as 0.21% (see text S11), but there is considerable uncertainty in this value because of uncertainty in the emission area.

In summary, we report a new type of NDR device, a nonsuspended device architecture that acts as an atomic-scale light emitter. The use of PECVD graphene permits graphene to be grown directly on the target substrate and opens the way to fabricate complementary metal-oxide semiconductor–compatible large-scale light-emitting graphene devices. This nanogap device can be used for new types of NDR electronics requiring high on-currents and high peak-to-valley voltage ratios.

# **MATERIALS AND METHODS**

#### PECVD growth of graphene

In our case, growth proceeds using RF (radio frequency) plasma of CH<sub>4</sub>. The growth substrates are 500- $\mu$ m-thick, 4-inch Si wafers with a 285-nm-thick SiO<sub>2</sub> layer. The growth temperature was 500°C at a heating rate of 10°C/min, and deposition time was 1 min in a mixture of methane [CH<sub>4</sub>, 2 standard cubic centimeter per minute (sccm)]

and hydrogen ( $H_2$ , 20 sccm), while the pressure was maintained at 10 mtorr. The gas mixtures were discharged at a power of 50 W for the specific growth time. The sample was cooled to room temperature at a cooling rate of 3°C/s by turning off the heater power.

#### **Device fabrication**

PECVD graphene on SiO<sub>2</sub>/highly p-doped Si substrate is used as a channel layer to make a light-emitting array. The 1  $\mu$ m-by-1  $\mu$ m graphene area for each pixel was patterned by dry etching using CHF3 and O2, while a liftoff process was used to define the electrodes. Liftoff method is used to pattern channel layer and electrodes. Poly(methyl methacrylate) (MicroChem PMMA, A4 495 and A2 950) was coated in 2000 and 1000 rpm for 1 min on the sample. Following this, the sample was baked on hot plate at 180°C for 2 min. For lithography, electron beam lithography (EBL) was used (Nano Neam, NB4). To avoid shorting between contact and interconnect layers, islands of insulating hydrogen silsesquioxane were created, which were patterned by EBL. To develop the pattern, isopropyl alcohol solution mixed with methyl isobutyl ketone as 3:1 stored under −5°C in the fridge was used. Cr/Pd/Au of 1 nm/30 nm/50 nm and Cr/Au of 1 nm/50 nm were deposited as metal electrodes in an electron beam evaporator. After this, liftoff was done in acetone for 1 hour. These lithography, deposition, and liftoff procedures were repeated for each layer.

#### **Device characterization**

Before packaging with wire bonding onto a 128-pin ball grid array package, we tested the devices in a vacuum chamber at  $10^{-4}$  to  $10^{-7}$  torr. For encapsulation, we bonded the chip carrier to 500-µmthick soda lime glass with ultraviolet (UV)–curable epoxy at  $10^{-5}$  torr. To measure electrical properties, a semiconductor analyzer (Agilent, B1500A) and a Keithley 2400 were used in a vacuum environment. The surface morphology of PECVD graphene was observed with an optical microscope and AFM with a silicon tip (model number is OTESPA-R3) from Bruker Co. Atomic bonding structure and photoluminescence in samples were observed through Raman spectroscopy (Renishaw, 532- and 405-nm laser; objective lens,  $100\times$ ). The stoichiometry of PECVD graphene and arrays was analyzed by XPS. EL was measured in a small vacuum chamber with a SpectraPro spectrometer having 1200 g/mm grating (Princeton Instrument Co.).

# **Packaging**

Some of the device, most notably the array device of Fig. 1D, is hermetically sealed in vacuum. This is done by sealing a cover slip on top of the ceramic chip carrier (128 pin, Spectrum Semiconductor Materials Inc.) using UV-curable epoxy (Epoxies Etc., 60-7170), which is subsequently cured at UV lamp for 1 min.

# **DFT calculation**

The Virtual Nanolab Atomistix Tool Kit was used for DFT-NEGF calculations. The density mesh cutoff is set as 100 Hartrees. K-point sampling is  $1 \times 1 \times 100$ . When plotting the I-V curves, we sweep voltage bias from 0 to 3 V with a 91-point grid and energy from -2 to 2 eV with 201 points. Bias can be calculated from the difference in the Fermi level on the two sides of the device structure. Zero energy is the average of the Fermi level on the two sides of the device. When calculating the transmission, we sweep the energy from -3 to 3 eV with a 601-point grid. Default parameters for the simulation are 2.09 Å between O and C, 3.70 Å between O and O, and 1.28 Å between C and C.

#### SUPPLEMENTARY MATERIALS

Supplementary material for this article is available at https://science.org/doi/10.1126/sciadv.abj1742

#### **REFERENCES AND NOTES**

- Y. D. Kim, H. Kim, Y. Cho, J. H. Ryoo, C.-H. Park, P. Kim, Y. S. Kim, S. Lee, Y. Li, S.-N. Park, Y. S. Yoo, D. Yoon, V. E. Dorgan, E. Pop, T. F. Heinz, J. Hone, S.-H. Chun, H. Cheong, S. W. Lee, M.-H. Bae, Y. D. Park, Bright visible light emission from graphene.
   Nat. Nanotechnol. 10. 676–681 (2015).
- C.-H. Lee, G.-H. Lee, A. M. van der Zande, W. Chen, Y. Li, M. Han, X. Cui, G. Arefe, C. Nuckolls, T. F. Heinz, J. Guo, J. Hone, P. Kim, Atomically thin p-n junctions with van der Waals heterointerfaces. *Nat. Nanotechnol.* 9, 676–681 (2014).
- X. Wang, H. Tian, M. A. Mohammad, C. Li, C. Wu, Y. Yang, T.-L. Ren, A spectrally tunable all-graphene-based flexible field-effect light-emitting device. *Nat. Commun.* 6, 7767 (2015)
- H. Zhang, W. Bao, Z. Zhao, J.-W. Huang, B. Standley, G. Liu, F. Wang, P. Kratz, L. Jing, M. Bockrath, C. N. Lau, Visualizing electrical breakdown and ON/OFF states in electrically switchable suspended graphene break junctions. *Nano Lett.* 12, 1772–1775 (2012).
- B. Standley, W. Bao, H. Zhang, J. Bruck, C. N. Lau, M. Bockrath, Graphene-based atomic-scale switches. *Nano Lett.* 8, 3345–3349 (2008).
- C. He, J. Li, X. Wu, P. Chen, J. Zhao, K. Yin, M. Cheng, W. Yang, G. Xie, D. Wang, D. Liu, R. Yang, D. Shi, Z. Li, L. Sun, G. Zhang, Tunable electroluminescence in planar graphene/ SiO<sub>2</sub> memristors. *Adv. Mater.* 25, 5593–5598 (2013).
- C. He, Z. Shi, L. Zhang, W. Yang, R. Yang, D. Shi, G. Zhang, Multilevel resistive switching in planar graphene/SiO<sub>2</sub> nanogap structures. ACS Nano 6, 4214–4221 (2012).
- L. Esaki, New phenomenon in narrow germanium p-n junctions. Phys. Rev. 109, 603-604 (1958).
- 9. S. M. Sze, K. K. Ng, Physics of Semiconductor Devices (John Wiley & Sons Inc., ed. 3, 2006).
- D. L. Klein, R. Roth, A. Lim, A. P. Alivisatos, P. L. McEuen, A single-electron transistor made from a cadmium selenide nanocrystal. *Nature* 389, 699–701 (1997).
- R. P. Puchert, F. Steiner, G. Plechinger, F. J. Hofmann, I. Caspers, J. Kirschner, P. Nagler, A. Chernikov, C. Schüller, T. Korn, J. Vogelsang, S. Bange, J. M. Lupton, Spectral focusing of broadband silver electroluminescence in nanoscopic FRET-LEDs. *Nat. Nanotechnol.* 12, 637–641 (2017).
- J. Kern, R. Kullock, J. Prangsma, M. Emmerling, M. Kamp, B. Hecht, Electrically driven optical antennas. *Nat. Photonics* 9, 582–586 (2015).
- R. Berndt, J. Gimzewski, P. Johansson, Inelastic tunneling excitation of tip-induced plasmon modes on noble-metal surfaces. *Phys. Rev. Lett.* 67, 3796–3799 (1991).
- Y. S. Kim, K. Joo, S.-K. Jerng, J. H. Lee, D. Moon, J. Kim, E. Yoon, S.-H. Chun, Direct integration of polycrystalline graphene into light emitting diodes by plasma-assisted metal-catalyst-free synthesis. ACS Nano 8, 2230–2236 (2014).
- A. C. Ferrari, D. M. Basko, Raman spectroscopy as a versatile tool for studying the properties of graphene. *Nat. Nanotechnol.* 8, 235–246 (2013).
- Y. S. Kim, K. Joo, S.-K. Jerng, J. H. Lee, E. Yoon, S.-H. Chun, Direct growth of patterned graphene on SiO<sub>2</sub> substrates without the use of catalysts or lithography. *Nanoscale* 6, 10100–10105 (2014).
- S. Berciaud, M. Y. Han, K. F. Mak, L. E. Brus, P. Kim, T. F. Heinz, Electron and optical phonon temperatures in electrically biased graphene. *Phys. Rev. Lett.* 104, 227401 (2010).
- W. Gao, P. Xiao, G. Henkelman, K. M. Liechti, R. Huang, Interfacial adhesion between graphene and silicon dioxide by density functional theory with van der Waals corrections. J. Phys. D Appl. Phys. 47, 255301 (2014).
- X. F. Fan, W. T. Zheng, V. Chihaia, Z. X. Shen, J.-L. Kuo, Interaction between graphene and the surface of SiO<sub>2</sub>. J. Phys. Condens. Matter 24, 305004 (2012).
- A. Delehouzé, F. Rebillat, P. Weisbecker, J.-M. Leyssale, J.-F. Epherre, C. Labrugère,
   G. L. Vignoles, Temperature induced transition from hexagonal to circular pits in graphite oxidation by O<sub>2</sub>. Appl. Phys. Lett. 99, 044102 (2011).
- M. Freitag, H.-Y. Chiu, M. Steiner, V. Perebeinos, P. Avouris, Thermal infrared emission from biased graphene. Nat. Nanotechnol. 5, 497–501 (2010).
- P. Vinchon, X. Glad, G. R. Bigras, R. Martel, L. Stafford, Preferential self-healing at grain boundaries in plasma-treated graphene. *Nat. Mater.* 20, 49–54 (2021).
- D. Solenov, K. A. Velizhanin, Adsorbate transport on graphene by electromigration. Phys. Rev. Lett. 109, 095504 (2012).
- J. H. Stathis, D. J. DiMaria, Identification of an interface defect generated by hot electrons in SiO<sub>2</sub>. Appl. Phys. Lett. 61, 2887–2889 (1992).
- V. E. Dorgan, M.-H. Bae, E. Pop, Mobility and saturation velocity in graphene on SiO<sub>2</sub>. Appl. Phys. Lett. 97, 082112 (2010).
- J. Moser, A. Bachtold, Fabrication of large addition energy quantum dots in graphene. Appl. Phys. Lett. 95, 173506 (2009).

# SCIENCE ADVANCES | RESEARCH ARTICLE

- A. Barreiro, H. S. J. van der Zant, L. M. K. Vandersypen, Quantum dots at room temperature carved out from few-layer graphene. Nano Lett. 12, 6096–6100 (2012).
- P. R. Berger, A. Ramesh, in Comprehensive Semiconductor Science and Technology (Elsevier, 2011), vol. 5 of Comprehensive Semiconductor Science and Technology, pp. 176–241; www.researchgate.net/publication/288207180\_Negative\_Differential\_Resistance\_ Devices and Circuits/link/5e38f557458515072d7d0400/download.
- D. Carrascal, V. M. García-Suárez, J. Ferrer, Impact of edge shape on the functionalities of graphene-based single-molecule electronics devices. *Phys. Rev. B* 85, 195434 (2012).
- 30. I. Wenåker, The spectrum of singly ionized oxygen, O II. Phys. Scr. 42, 667–684 (1990).
- K. A, R. Yu, R. J., N. A. Team, NIST Atomic Spectra Database (ver. 5.5.6) (2018); https://physics.nist.gov/asd.
- 32. V. I. Kogan, V. S. Lisitsa, G. V. Sholin, Spectral-Line Broadening in a Plasma, in *Reviews of Plasma Physics* (Springer, 1987), vol. 13, pp. 261–334.
- 33. R. Berndt, J. Kröger, N. Néel, G. Schull, Controlled single atom and single molecule contacts. *Phys. Chem. Chem. Phys.* **12**, 1022–1032 (2009).
- J. J. Camacho, M. Santos, L. Díaz, J. M. L. Poyato, Optical emission spectroscopy of oxygen plasma induced by IR CO<sub>2</sub> pulsed laser. J. Phys. D Appl. Phys. 41, 215206 (2008).

Acknowledgments: We thank S.-K. Jerng and S.-H. Chun in the Sejong University for synthesized CVD graphene, K. Barmak and A. Zangiabadi in the Department of Applied Physics and Applied Mathematics of Columbia University for TEM, and A. N. Pasupathy and A. Kerelsky in the Department of Physics of Columbia University for STM and AFM. We thank C. R. Dean in the Department of Physics of Columbia University for helpful discussions.

Funding: This work was supported by SRC/NRI under the INDEX program. Y.D.K. acknowledges support from the NRF of Korea (2021R1A2C2093155 and 2021M3H4A1A03054856) and a grant from the Kyung Hee University (KHU-20211033). Author contributions: Conceptualization: H.K., J.H., and K.L.S. Methodology: H.K. and Y.D.K. Investigation: T.W., Q.C., and I.P.H. Visualization: H.K. and Y.D.K. Supervision: J.H., J.G., and K.L.S. Writing—original draft: H.K. Writing—review and editing: H.K. and K.L.S. Competing interests: The authors declare that they have no competing interests. Data and materials availability: All data needed to evaluate the conclusions in the paper are present in the paper and/or the Supplementary Materials.

Submitted 9 May 2021 Accepted 29 November 2021 Published 21 January 2022 10.1126/sciadv.abj1742

# **Science**Advances

# Electroluminescence of atoms in a graphene nanogap

Hyungsik KimYoung Duck KimTong WuQingrui Caolrving P. HermanJames HoneJing GuoKenneth L. Shepard

Sci. Adv., 8 (3), eabj1742. • DOI: 10.1126/sciadv.abj1742

View the article online

https://www.science.org/doi/10.1126/sciadv.abj1742

**Permissions** 

https://www.science.org/help/reprints-and-permissions

Use of this article is subject to the Terms of service